MIT Open Access Articles

Inverted metamorphic AlGaInAs/GaInAs tandem thermophotovoltaic cell designed for thermal energy grid storage application

Massachusetts Institute of Technology

DSpace@MIT

Inverted Metamorphic AlGaInAs/GaInAs Tandem Thermophotovoltaic Cell Designed for Thermal Energy Grid Storage Application

Kevin L. Schulte,[1,a] Ryan M. France,[1] Daniel J. Friedman,[1] Alina D. LaPotin,[2] Asegun Henry,[2] and Myles A. Steiner[1]

[1]*National Renewable Energy Laboratory, Golden, Colorado 80401, USA*

[2]*Massachusetts Institute of Technology, Cambridge, Massachusetts 80401, USA*

[a)]**Author to whom correspondence should be addressed**: kevin.schulte@nrel.gov

ABSTRACT

We demonstrate an inverted metamorphic multijunction (IMM) photovoltaic cell comprising lattice-mismatched 1.2 eV AlGaInAs and 1.0 eV GaInAs junctions optimized for high-temperature thermophotovoltaic (TPV) applications. This device differs from traditional IMM solar cells because the mismatched junctions are grown at a single lattice constant. This architecture enables removal of the compositionally graded buffer which otherwise filters light from the junctions below and absorbs sub-bandgap light via free-carrier absorption. Sub-bandgap absorption dramatically reduces the efficiency of TPV systems using high reflectivity cells to enable bandedge spectrum filtering. Three components required development to enable this device: 1) a lattice-mismatched 1.2 eV AlGaInAs junction, 2) a metamorphic contact layer grown after the graded buffer, and 3) a transparent tunnel junction that sits in front of the 1.0 eV GaInAs junction. Growth conditions that minimize oxygen defect incorporation maximize AlGaInAs cell quality, enabling a 0.41 V bandgap open circuit voltage offset at 22 mA/cm^2 under AM1.5D. A mismatched GaInAs:Se layer is developed as a low resistance contact. Lastly we develop a GaAsSb:C/GaInP:Se tunnel junction suitable for high-power densities with more transparency than the GaAsSb:C/GaInP:Se structure used in past IMM cells. We characterize the tandem device under a high-intensity spectrum that approximates the emission from a 2150 °C blackbody radiator and deduce a projected ideal TPV efficiency of 39.9% at ~30% of the blackbody irradiance, and 36% ideal TPV efficiency under the full 118 W/cm^2 irradiance. Improvements to the back-surface reflectivity and series resistance are expected to increase the ideal TPV efficiency well above 40%.

I. INTRODUCTION

Metamorphic III-V epitaxy enables flexible design of multijunction devices by using compositionally graded buffers to shift the lattice constant, enabling access to a palette of materials with a wide range of properties and bandgaps (E_G).[1] The best example of this technology is the inverted metamorphic multijunction (IMM) solar cell, grown by organometallic vapor phase epitaxy (OMVPE). The IMM recently achieved 47.1% conversion efficiency for a six-junction embodiment under concentrated light.[2] Traditionally, IMM designs utilize one graded buffer per mismatched junction as shown in Fig. 1(a), left. For example, the six-junction IMM contains three mismatched $Ga_{1-x}In_xAs$ junctions and three $Ga_{1-x}In_xP$ graded buffers. This design is used because metamorphic $Ga_{1-x}In_xAs$ can be grown on GaAs with higher quality than any

other alloy in the bandgap range between 0.7-1.4 eV, and each $Ga_{1-x}In_xAs$ composition comprising the bottom three junctions possesses a different lattice constant.[1,3] The graded buffers are left in the device because they are transparent to the photons intended to be absorbed in the underlying junctions, and thus do not reduce device performance in the intended *solar* photovoltaic application through parasitic absorption of the photons relevant for solar cells.

The IMM's versatility makes it potentially useful for non-solar applications. Recently, a thermal energy storage system using mechanically pumped molten Si as the storage medium, with electricity re-generation from rear-reflective two-junction thermophotovoltaic (TPV) cells was proposed.[4] The system has attractive economics that rival pumped hydroelectricity, and is a contending option for addressing the grid storage problem for intermittent renewable sources.[5] One key aspect of the technology is the system's roundtrip efficiency, which depends
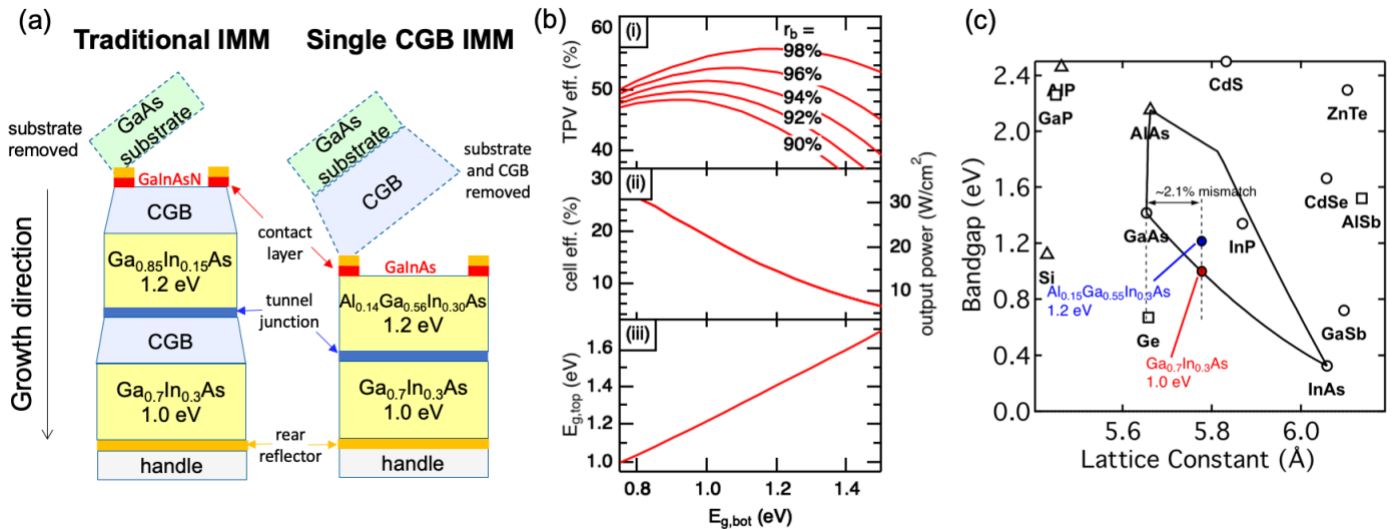
Fig. 1 (a) Illustration of a traditional inverted metamorphic multijunction (IMM) solar cell with two compositionally graded buffers (CGBs) and two metamorphic junctions and an IMM with one CGB and two metamorphic junctions. (b) TPV system efficiency (i), tandem efficiency and output power (ii), and optimal top cell band gap (iii) as a function of bottom cell band gap assuming a 2150 °C radiator. (c) Bandgap vs. lattice constant diagram depicting the single CGB approach.

almost wholly on the TPV efficiency. Thus, the development of highly efficient multijunction TPV cells could play a critical role in enabling energy storage, renewable penetration and ultimately climate change mitigation.

Fig. 1(b) displays an analysis of this system for a 2150 °C blackbody radiator, showing (i) the TPV system efficiency for varying sub-bandgap reflectivity (r_b), (ii) cell efficiency (left axis) and output power (right axis), and (iii) optimal top cell band gap as a function of bottom cell band gap. 2150 °C is chosen as the midpoint between the Si hot and "cold" reservoirs.[4] This temperature is much higher than the 1000-1500 °C range more traditionally associated with TPV applications, necessitating a significantly higher-bandgap device design than for traditional TPV devices.[6] The model assumes optically thick junctions with dark currents corresponding to a bandgap-open circuit voltage (V_{OC}) offset (W_{OC}) of $W_{OC} = E_G/e - V_{OC} = 0.4$ V at a reference short-circuit current density (J_{SC}) = 16 mA/cm^2. This value of W_{OC} is relatively conservative and implies no photon recycling and no dependence on r_b. The TPV efficiency is higher than the cell efficiency because unconverted sub-bandgap photons that are reflected back to the radiator are not lost, but instead their energy is reused. Cell-level efficiency and output power are maximized using low band gaps that absorb and convert a greater portion of light from the radiator, but the *TPV efficiency* is maximized at higher bandgaps, resulting in a tradeoff. A 1.2/1.0 eV tandem provides a good balance of TPV efficiency and output power, if a sub-bandgap reflectivity >90% and preferably near 98% can be obtained. We note that as the radiator cools, the cell and TPV efficiencies, as well as the optimal bandgaps, could change as the emission spectrum redshifts. An energy yield optimization that takes into account the time dependence of the radiator temperature will be required to optimize the TPV system, but this analysis is beyond of the scope of the present study.

In analogy to the traditional IMM solar cell approach, a design with two $Ga_{1-x}In_xP$ graded buffers and two $Ga_{1-x}In_xAs$

junctions (Fig. 1(a), left) is an obvious starting point for this TPV application; however, some redesign is required to optimize it for TPV. The thick, highly-doped graded buffer is a potential source of parasitic sub-bandgap absorption by free-carriers[7,8] and/or dislocations.[9,10] These potential sources of absorption are of major concern for TPV applications, because reflection of sub-bandgap light back to the radiator is critical for TPV system conversion efficiency, and is also important for thermal management. The former point is highlighted in panel (i) in Fig. 1(b), which shows dramatic decreases in TPV system efficiency with decreasing sub-bandgap reflectivity. Sub-bandgap light that is absorbed in the device obviously cannot be reflected back to the radiator, reducing TPV efficiency. Parasitic absorption of above-bandgap light in the grade is also an issue in this design, because there are no absorbing junctions above the grade as in an IMM solar cell. The solution to both challenges is to grow a device with a single graded buffer that is removed during processing (Fig. 1(a), right) – a novel enabling feature of this device architecture. The resultant device, now optimized for TPV, requires development of a mismatched contact layer grown after the grade, a new material for the top junction, and a transparent tunnel junction.

Growth of a multijunction device with a single grade requires the use of quaternary materials such as $Ga_{1-x}In_xAs_yP_{1-y}$ or $Al_yGa_{1-x-y}In_xAs$ for the top junction, to provide an extra degree of freedom with which to change the band gap because the lattice constants of the two junctions are now constrained to be the same (Fig. 1c). Phase separation limits the performance of metamorphic $Ga_{1-x}In_xAs_yP_{1-y}$ grown by OMVPE,[3,11] and that material system is further complicated by difficulties related to non-linear, temperature-dependent, incorporation of As vs. P. Metamorphic $Al_yGa_{1-x-y}In_xAs$ is used successfully as a graded buffer material, and is less prone to phase separation as long as x_{In} remains below ~0.35,[12] making it a more promising candidate. The introduction of oxygen and other defects concomitant with the use of Al[13-15] must be addressed in order to use $Al_yGa_{1-x-y}In_xAs$ as a minority carrier device layer,

however. Reports of high-quality lattice-matched AlInAs[16,17] and AlGaAs[3,13,14] solar cells exist, and metamorphic $Al_yGa_{1-x-y}In_xAs$ is used in devices such as upright metamorphic solar cells[18-20], but materials studies of this alloy are limited.

In this work, we demonstrate a two junction 1.2/1.0 eV $Al_{0.14}Ga_{0.57}In_{0.29}As/Ga_{0.70}In_{0.30}As$ solar cell with a single, removable graded buffer. This device required the development of three new components in order to adapt the traditional IMM cell for TPV applications. First, we show a detailed growth optimization of an $Al_{0.14}Ga_{0.57}In_{0.29}As$ top cell. Then we develop a mismatched contact layer that is placed after the graded buffer, enabling the grade's removal. Lastly, we show improvements to the baseline tunnel junction to make it more transparent yet still robust at high device current. High-intensity device measurements conducted under a simulated high-intensity 2150 °C-radiator TPV system spectrum[4] are used to characterize the device performance. We combine these device measurements with measurements of the broadband device reflectance to estimate an ideal TPV device efficiency. Finally, we analyze the sensitivity of the TPV efficiency to sub-bandgap reflectance and to series resistance; with this analysis, we present a roadmap to significantly improved efficiencies in future generations of this device structure.

II. EXPERIMENTAL

All devices were grown in an inverted fashion by atmospheric-pressure OMVPE with standard precursors. Substrates were Si-doped (100) GaAs offcut 2° towards the (111)B plane. Step-graded $Ga_{1-x}In_xP$ buffer layers were used to bridge the 2.1% lattice-mismatch between the GaAs substrate and $Ga_{0.70}In_{0.30}As$. The deposition temperature (T_D) of the grade was 675 °C, the growth rate was ~ 7 µm/h, the V/III ratio was 450, and the strain-grading rate was 1%/µm. At the end of the grade a one-µm strain "overshoot" layer was grown, followed by a one-µm "step-back" layer lattice-matched to the in-plane lattice constant of the overshoot.[21] The lattice-matched GaInNAs or lattice-mismatched GaInAs contact layers are described later. Both the $Al_{0.14}Ga_{0.57}In_{0.29}As$ and $Ga_{0.70}In_{0.30}As$ solar cells were front homojunctions, with a 0.1 µm n-type emitter, 0.1 µm i-layer, and 3 and 2.5 µm thick p-type base layers, respectively. $Ga_{0.32}In_{0.78}P$ cladding layers were used in front and in back of each cell. A thin, highly p-doped (>1x10^{19} cm^{-3}), 0.1 µm $Al_{0.40}Ga_{0.31}In_{0.29}As$ layer was deposited after the back GaInP cladding layer. The $Ga_{0.70}In_{0.30}As$ cells were grown at T_D = 650 °C with a V/III ratio of 24. We studied the effect of T_D and V/III on the performance of the $Al_{0.14}Ga_{0.57}In_{0.29}As$ cells, and these parameters varied between 650-725 °C and 23-264, respectively. The growth rate for both junctions was ~6 µm/h. Oxygen concentration [O] was measured in $Al_{0.14}Ga_{0.57}In_{0.29}As$ layers by secondary ion mass spectrometry. Two-junction $Al_{0.14}Ga_{0.57}In_{0.29}As/Ga_{0.70}In_{0.30}As$ devices with varying tunnel junction structures were grown. Tunnel junctions comprised either $GaAs_{0.73}Sb_{0.27}:C/Ga_{0.70}In_{0.30}As:Se$, $GaAs_{0.73}Sb_{0.27}:C/Ga_{0.22}In_{0.78}P:Se$, or $Al_{0.30}Ga_{0.41}In_{0.29}As:C/Al_{0.30}Ga_{0.41}In_{0.29}As:Se$, each layer being ~50 nm thick. Se-doping was achieved with hydrogen selenide while carbon

tetrachloride was used as a carbon dopant.

Devices were processed as in ref. 22 with electroplated concentrator-style Au/Ni front grids and a reflective, broad-area electroplated Au back contact. Device active area excluding busbars was 0.10 cm^2 and total device area was 0.11 cm^2. A MgF_2/ZnS bilayer anti-reflection coating was applied to a select device by thermal evaporation. External quantum efficiency (EQE) was measured using monochromated light. Above-bandgap reflectance was measured concurrently with EQE using a calibrated photodiode and used to calculate internal quantum efficiency (IQE). Light emitting diodes were used to limit each subcell of multijunction devices enabling measurement of individual subcell QE. EQE was used along with a reference cell to calculate spectral mismatch and calibrate a Xe-arc lamp source to a one-sun (1 kW/m^2) condition under the standard ASTM G173 AM 1.5 Direct (AM1.5D) solar spectrum, under which current density-voltage (*J-V*) curves were measured. *J-V* curves were also measured in the dark. We note that the AM1.5D spectrum overdrives the top cell of the proposed tandem relative to the TPV spectrum, and is ~1000x lower in total irradiance, but provides a convenient benchmark for single-junction cell development. Contact resistance was measured from diagnostic structures by the transfer length method. Injection-dependent external radiative efficiency, defined as the ratio of emitted photon flux to injected current density,[23] was determined from electroluminescence measurements of select devices and converted to junction voltage via the reciprocity thorem.[24,25] Flash *I-V* measurements were conducted under an uncorrected spectrum using a high-intensity pulsed solar simulator (HIPSS) with a Xe-arc lamp to characterize tunnel junction performance at high current-density. Flash *I-V* measurements, further described in section III.D, were also performed under a hypothetical TPV spectrum represented by the emission of a 2150 °C radiator[4] using a tunable high-intensity pulsed solar simulator (T-HIPSS). All *J-V* and *I-V* measurements at one-sun and under concentration were conducted at 25 °C. We note that cells operating under real TPV conditions will likely be hotter, but this standard temperature provides a convenient baseline condition for broader comparison with other PV devices. We further note that a real TPV system will employ water-cooling[4] to limit the total temperature increase, and that the device is readily re-optimized for higher temperature operation[26] with small changes in the junction bandgaps. Estimation of a TPV system efficiency requires knowledge of the broadband device reflectance. Reflectance at wavelengths <1.24 µm was collected during EQE measurement, while reflectance >2.50 µm was measured by normal-incidence Fourier transform infrared (FTIR) microscopy. The spot size for this measurement was adjustable between 10 and 300 µm, enabling direct measurement of the processed tandem device between the grid fingers. The FTIR was calibrated using a high-reflectivity gold standard. Reflectivity from 1.24-2.50 µm was estimated using an optical model as detailed in the Appendix.
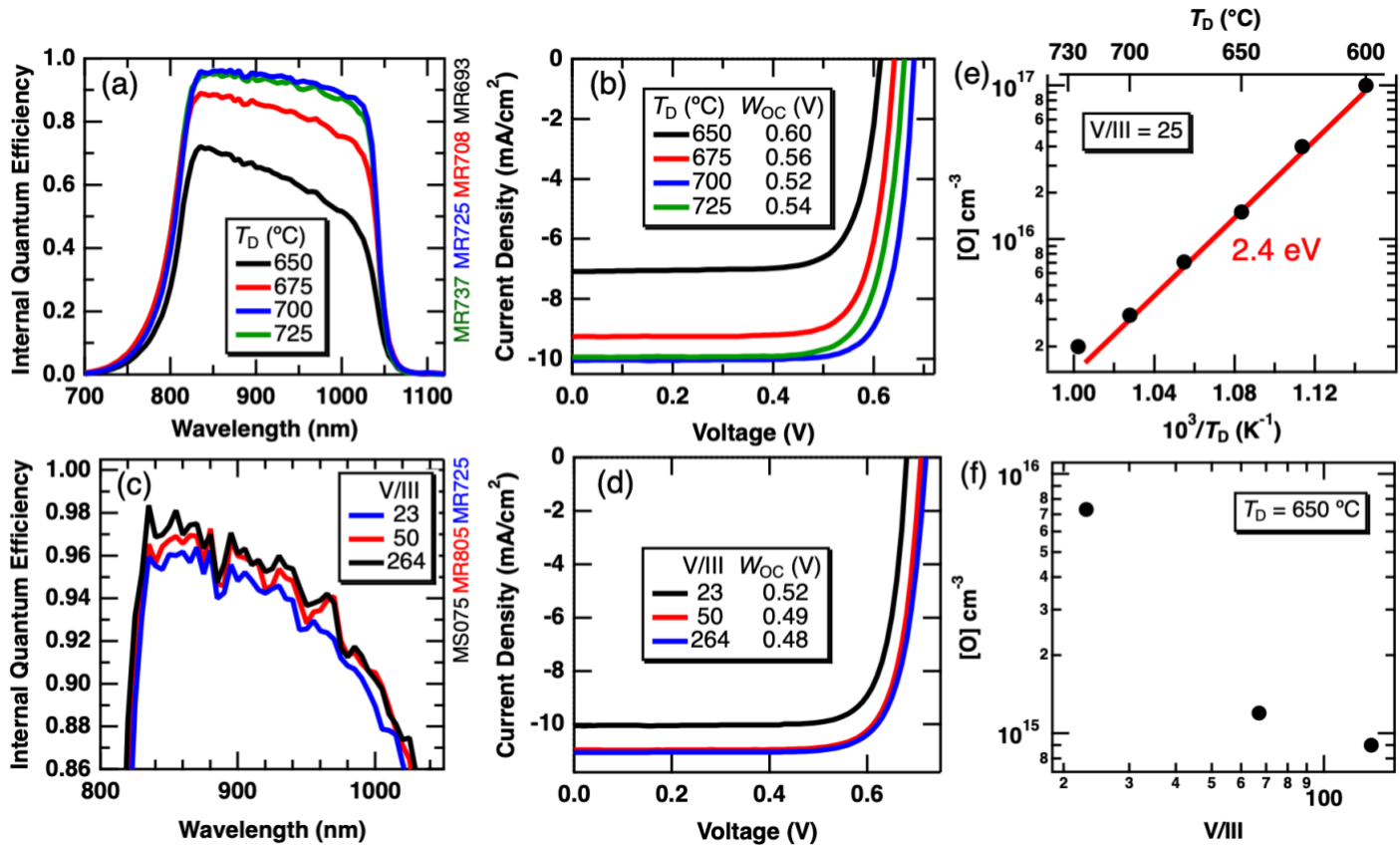
III. RESULTS AND DISCUSSION

Fig. 2 Internal quantum efficiency and current density-voltage curves for ~1.2 eV $Al_{0.14}Ga_{0.57}In_{0.29}As$ solar cells grown with varying deposition temperature at constant V/III ratio = 23, (a) and (b), and varying V/III ratio with constant deposition temperature = 700 °C, (c) and (d). Oxygen concentration in $Al_{0.14}Ga_{0.57}In_{0.29}As$ as a function of deposition temperature (e) and V/III (f).

A. ALGAINAS CELL DEVELOPMENT

First, we studied the effect of growth conditions on the quality of metamorphic 1.2 eV $Al_{0.14}Ga_{0.57}In_{0.29}As$ material intended for the top junction of the proposed 2J device. Fig. 2(a) and (b) show the IQE and one-sun light J-V for single-junction $Al_{0.14}Ga_{0.57}In_{0.29}As$ devices grown with varying T_D and a constant V/III = 23. The maximum IQE increases from ~72% at T_D = 650 °C up to ~96% at 700 °C. The IQE decreases slightly as T_D increases further to 725 °C. As expected, the trends in J-V short-circuit current (J_{SC}) match those in the IQE, increasing with temperature up to 700 °C, then decreasing at 725 °C. Similarly, V_{OC} increases from 0.613 V to 0.680 V between 650 and 700 °C then decreases to 0.660 at 725 °C. The bandgap-V_{OC} offset (W_{OC}), an indicator of the material quality, is listed in the figure legend. Fig. 2(c) and (d) show the IQE and J-V for $Al_{0.14}Ga_{0.57}In_{0.29}As$ devices grown with varying V/III and a constant T_D = 700 °C. The maximum IQE increases slightly with V/III, up to ~98% at the highest V/III of 264. J_{SC} and V_{OC} also increase with V/III, with V_{OC} peaking at 0.720 V at the highest V/III, corresponding to a W_{OC} of 0.48 V.

The incorporation of oxygen in Al-containing III-V materials is a common issue,[27] due to the large strength of the Al-O bond.[28] Oxygen forms a deep level defect in III-V materials, and its presence reduces the performance of minority carrier devices such as solar cells.[14,15,29] We performed secondary ion mass spectrometry on metamorphic $Al_{0.14}Ga_{0.57}In_{0.29}As$ as a

function of T_D and V/III in order to understand oxygen incorporation in our devices. Fig. 2(e) and (f) show the measured [O] as a function of T_D with constant V/III and V/III with constant T_D, respectively. [O] decreases exponentially with T_D, from $1x10^{17}$ to $2x10^{15}$ cm^{-3}, as T_D increases from 600 to 725 °C. An effective activation energy, which likely encompasses various adsorption and reaction processes, of 2.4 eV is calculated. This is significantly larger than an effective energy found for OMVPE of $Al_{0.3}Ga_{0.7}As$.[27] The trend in [O] vs. T_D correlates closely with the improvement in V_{OC} and QE with T_D, suggesting that reductions in [O] are at least partially responsible for the device improvement. However, it is unclear why the device performance decreased above T_D = 700 °C as [O] continued to decrease. Likely some other aspect of the material quality degraded at those temperatures. [O] also decreases strongly as a function of V/III, dropping nearly an order of magnitude as V/III increases from 25 to 67 for samples grown at T_D = 650°C. [O] decreases only slightly with further V/III increase to 134. These trends in [O] with V/III correlate closely with device performance as a function of V/III, with the W_{OC} decreasing by 30 mV between V/III = 23 and 67, but only improving 10 mV more between V/III = 67 and 264. These results suggest that reduced [O] concentration is driving the performance improvement with increasing V/III. We note that, while the source of oxygen contamination in our reactor is presently unclear, the [O]-reduction methods demonstrated here translate to other OMVPE growth systems.
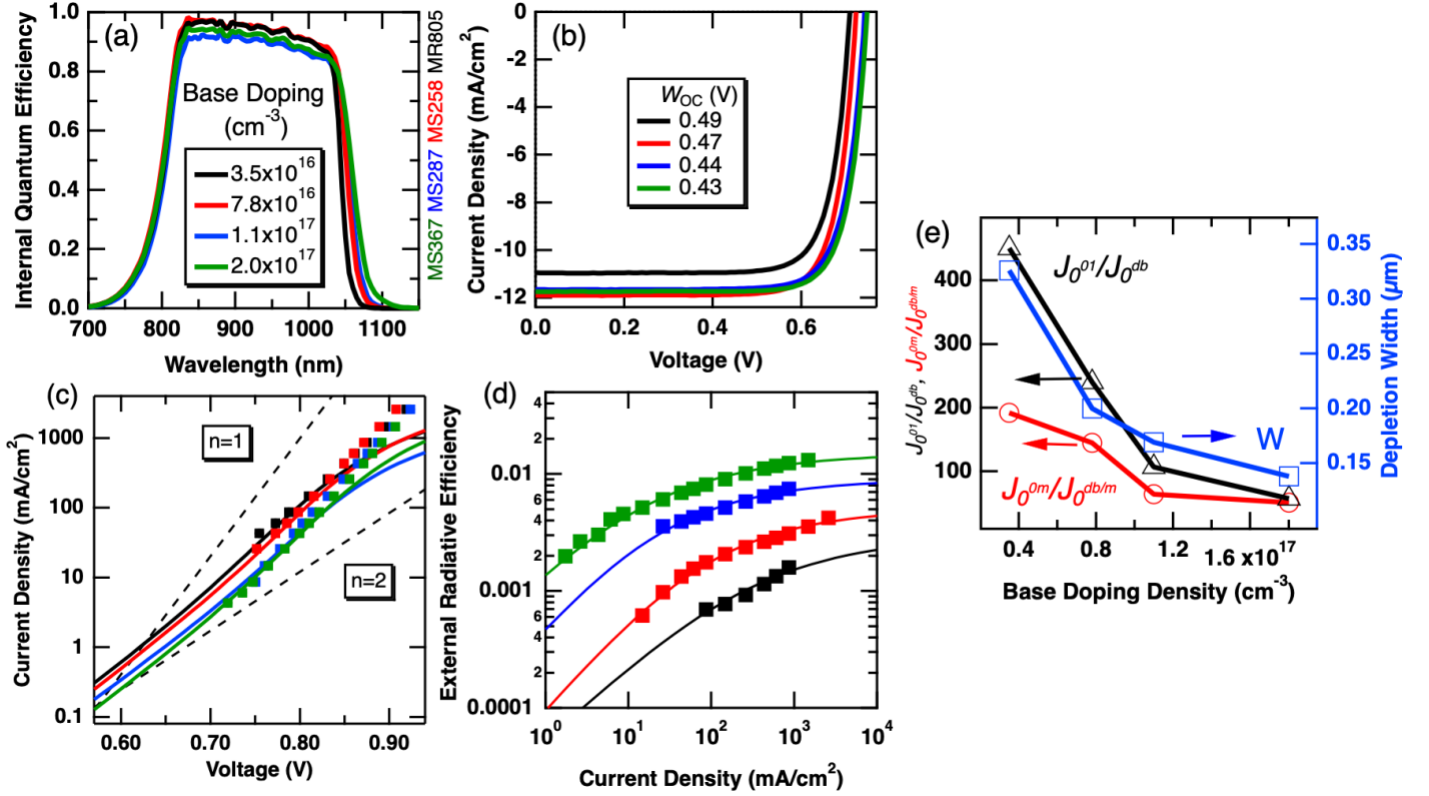
Fig. 3   Internal quantum efficiency (a) and light current density-voltage (b) for metamorphic Al$_{0.14}$Ga$_{0.57}$In$_{0.29}$As solar cells with varied base doping. Dark current density-voltage (c) and electroluminescence external radiative efficiency (d) of these cells. Current density-voltage extracted from electroluminescence is plotted as points in (c). (e): Results of external radiative efficiency and dark current fitting analysis using 2-diode model to extract J_0^{01}/J_0^{db} and $J_0^{0m}/J_0^{db/m}$, the ratios of dark current in the n=1 and n=m device regions to those derived for perfect junctions in the detailed balance limit (left axis) and junction depletion width, W, (right axis) as a function of doping density.

The emitter and base doping density vary as a function of V/III and T_D, though we did not attempt to control these parameters in these initial sets of experiments. The base doping decreased from 1.0×10^{17} to 2.1×10^{16} cm^{-3} as temperature increased from 650 to 725 °C. It is possible that part of the improvement in IQE with temperature could be due to an increasing minority carrier diffusion length with decreasing doping density. However, the concurrent increase in V_{OC} suggests that the improvement is due to reduced defect density, because decreasing doping density increases the J_{01} component of the dark current, which should decrease V_{OC}.[30] To further clarify the effect of base doping density on device performance, we grew a series of Al$_{0.14}$Ga$_{0.57}$In$_{0.29}$As devices with varying base dopant flow rate at constant T_D and V/III. Fig. 3 (a)-(b) shows the effect of base doping density on IQE and J-V performance of Al$_{0.14}$Ga$_{0.57}$In$_{0.29}$As devices grown at 700 °C with V/III = 67. The IQE decreases somewhat, though not linearly, with increasing base doping from 3.5×10^{16} to 2.0×10^{17} cm^{-3}. The absorption edge in the IQE (and EQE, not shown) becomes more gradual with doping density and shifts to longer wavelength, implying that the bandgap decreases with base doping density. The reason for the decrease in bandgap is presently unclear. The V_{OC} increases from 0.71 to 0.75 V with doping density, corresponding to a W_{OC} decrease by 60 mV. The one-sun W_{OC} of the cell with 1.1×10^{17} cm^{-3} doping rapidly decreases to 0.41 V as the J_{SC} increases to 22 mA/cm^2 with removal of the graded buffer (described in the next section). We

analyzed the dark J-V and electroluminescence from these devices to better understand the improvement in W_{OC} with base doping. Fig. 3(c) shows the dark J-V as curves, with electroluminescence-derived J-V plotted as points and (d) shows the electroluminescence external radiative efficiency for these devices. The curves in (d) are fits of the external radiative efficiency to the generalized optoelectronic model of Geisz et al.,[24] which uses a two-diode model to characterize the device. The model also includes fitting to the dark J-V. Fitting of these data allow extraction of the parameters J_0^{01}/J_0^{db} and $J_0^{0m}/J_0^{db/m}$ which represent the dark current-densities in the quasi-neutral and space charge regions of the device, respectively, normalized to the dark current-densities calculated in these regions for a perfect junction using the detailed balance model.[31] m is the ideality factor of the second diode, which is usually assumed to be two, though in the present case is 1.7-1.8 based on fits to the dark J-V. J_0^{01}/J_0^{db} is inversely related to doping density, whereas $J_0^{0m}/J_0^{db/m}$ is not dependent on doping density to first order.[30] Fig. 3(e) plots these fit parameters as a function of base doping. We see that both J_0^{01}/J_0^{db} and $J_0^{0m}/J_0^{db/m}$ decrease strongly with base doping, implying that both components of the diode current are impacted by the base doping density. The explanation for this trend is straightforward in the case of J_0^{01}/J_0^{db} because of the inverse dependence on doping density.[30] We hypothesize that the decrease in $J_0^{0m}/J_0^{db/m}$ with doping density is due to narrowing of the
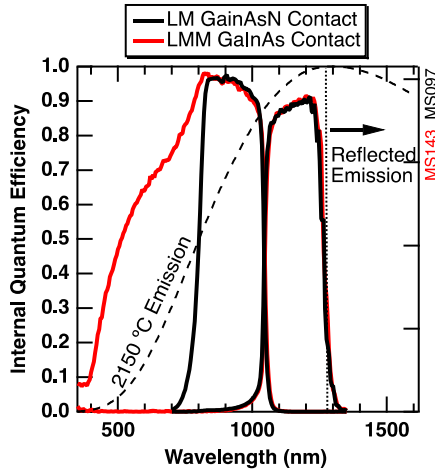
Fig. 4 Internal quantum efficiency for tandem solar cells with different contact layer materials. The graded buffer was removed in the GaInAs case.

TABLE I
Comparison of Contact Layers

Contact Type	ρ_C $(\Omega \cdot CM^2)$	R_{Sheet} after removal $(\Omega / \bullet)$	ρ_{Series} $(\Omega \cdot CM^2)$	Top/Bottom Cell Voltage @ 100 mA/cm^2 (V)
GaInAsN	1.2×10^{-4}	10	0.090	0.81/0.67
GaInAs	5×10^{-5}	151	0.050	0.80/0.67

Specific contact resistance (ρ_C), sheet resistance after contact removal (R_{Sheet}), specific series resistance (ρ_{Series}), and electroluminescence derived top and bottom junction voltages for tandems with varying contact types.

depletion width (W). Given that there is oxygen present in these Al-containing materials, and that oxygen is a deep level defect in III-Vs, it follows that we can drive down $J_0^{0m}/J_0^{db/m}$ by narrowing W with increasing base doping density. For reference, W, calculated from the zero-bias capacitance and the assumption that the p-n junction behaves as a parallel-plate capacitor, is plotted on the right axis of Fig. 3(e). The trend in $J_0^{0m}/J_0^{db/m}$, which should have a direct dependence on W,[30] correlates with the trend in W providing validation for this hypothesis.

B. MISMATCHED CONTACT DEVELOPMENT

The traditional IMM structure uses a Se-doped $Ga_{0.93}In_{0.07}As_{0.97}N_{0.03}$ contact that is lattice-matched to GaAs. The incorporation of In and N into GaAs reduces the bandgap, and increases the electron concentration in the material.[32] Furthermore, the rate of Se out-diffusion is dramatically reduced by the incorporation of N.[33] This is an important consideration during an inverted OMVPE growth where the contact layer, grown early in the stack, is subjected to the annealing load of the subsequent layers. Out-diffusion of dopant increases the metal-semiconductor contact resistance, decreasing the fill factor (FF) of the device.

To facilitate the removal of the grade, the contact layer must

be grown after the grade, instead of before it. GaInAsN is again a possible candidate material for the contact layer at the mismatched lattice-constant, but given the difficulty growing III-V-N materials even in a lattice-matched condition it is preferable to avoid this material. $Ga_xIn_{1-x}As$ has many desirable properties for a contact layer material, given its high electron effective mass and relatively low bandgap (1.0 eV) at the lattice constant of interest. The fact that the contact is grown after the grade somewhat reduces the annealing load as well. We developed a two-step $Ga_{0.70}In_{0.30}As$ contact with a highly-Se-doped 0.1 µm-thick region grown at 550 °C, and a lower-doped 0.2 µm-thick region grown at 700 °C, which matches the growth temperature of the top junction. Fig. 4 shows the IQE of two $Al_{0.14}Ga_{0.57}In_{0.29}As/Ga_{0.70}In_{0.30}As$ tandem devices grown with different contacts. The emission from a 2150 °C radiator is plotted on the right axis as a broken line for reference. One tandem features a $Ga_{0.93}In_{0.07}As_{0.97}N_{0.03}$ contact grown in front of the grade, lattice-matched to GaAs, while the other uses the two-step $Ga_{0.70}In_{0.30}As$ contact grown after the graded buffer, lattice-matched to the tandem. In the latter case, the graded buffer is removed. The removal of the grade considerably increases short-wavelength collection in the IQE, including portions of the 2150 °C spectrum the grade would otherwise absorb parasitically. Table I compares the contacts in terms of resistance and material quality metrics. The specific contact resistance of the mismatched $Ga_{0.70}In_{0.30}As$ is actually lower than that of the $Ga_{0.93}In_{0.07}As_{0.97}N_{0.03}$ contact, with a value of 5×10^{-5} vs. 1.2×10^{-4} $\Omega \cdot cm^2$. The sheet resistance after contact removal increases from 10 to 151 $\Omega /\bullet$ because the current no longer can spread in the thick grade. Despite this increase, the overall series resistance, determined by fitting of the fill factor obtained from flash concentrator measurements,[24] was lower for the GaInAs contact (0.050 $\Omega \cdot cm^2$ vs. 0.090 $\Omega \cdot cm^2$). Thus, the contact resistance is more limiting than the sheet resistance. The IQE heights for each junction are identical in both cases, and the junction voltages measured by electroluminescence listed in Table I are nearly identical as well. These results show that the material quality of the tandem is unaffected by the implementation of the mismatched contact and removal of the grade.

C. TUNNEL JUNCTION DEVELOPMENT

The third aspect of the device that must be addressed in moving to a single-grade design is the tunnel junction. We have previously developed a lattice-mismatched $GaAs_xSb_{1-x}:C/Ga_{1-x}In_xAs:Se$ tunnel junction for solar IMM devices[2,34] that is grown *after* the $Ga_{1-x}In_xAs$ junction at each lattice constant. There is no parasitic absorption in the tunnel junction in that structure as a consequence of this arrangement, assuming optically thick junctions. In the single-grade design considered in this work, the tunnel junction must be placed *in front of* the 1.0 eV $Ga_{0.70}In_{0.30}As$ cell, meaning that the tunnel junction will parasitically absorb photons if it contains layers with bandgaps below the 1.2 eV top cell bandgap, as the baseline $GaAs_xSb_{1-x}:C/Ga_{1-x}In_xAs:Se$ tunnel junction does.

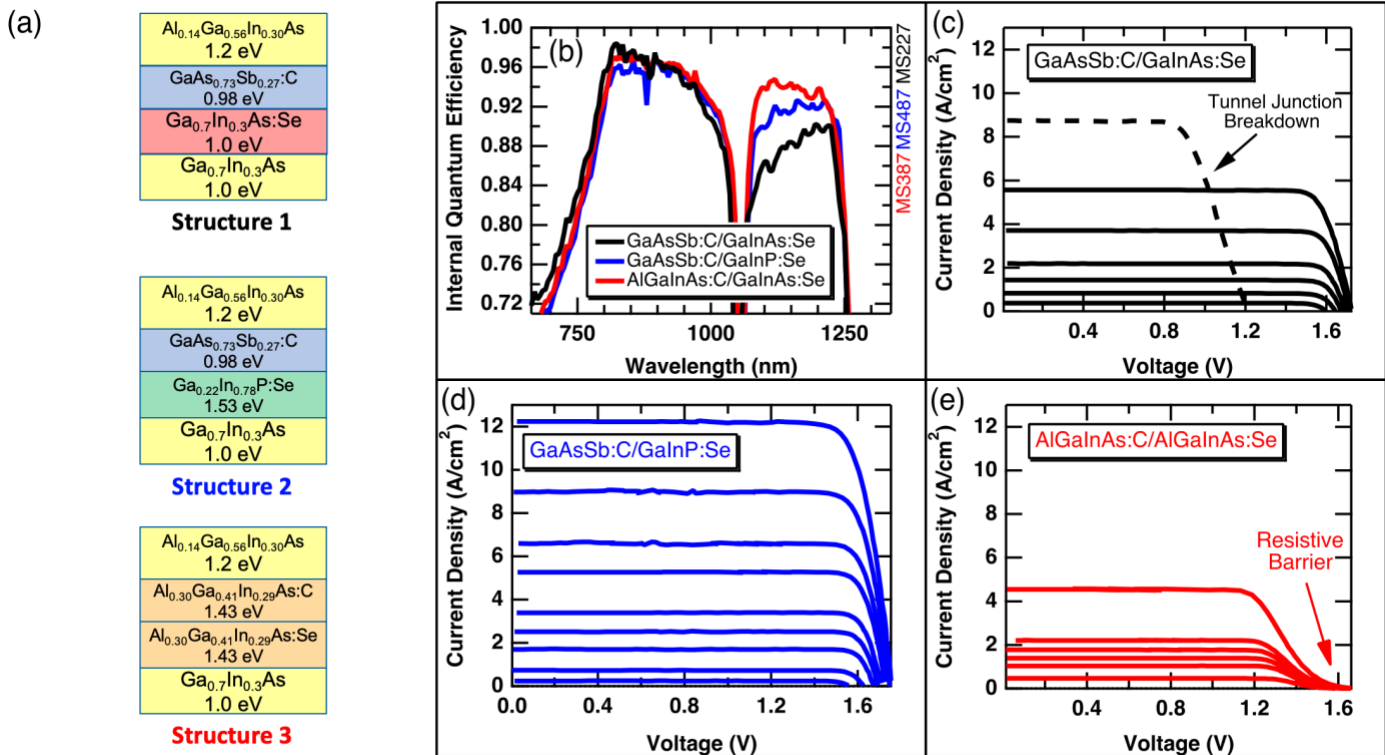We compared the effect of three different tunnel junction

Fig. 5 (a): Tunnel junction structures tested in this study. (b) Internal quantum efficiency of $Al_{0.14}Ga_{0.57}In_{0.29}As/Ga_{0.70}In_{0.30}As$ tandems with the three different tunnel junction structures of (a). (c)-(e): Current density-voltage curves at varying concentration level for each tandem device.

structures on tandem performance. Fig. 5(a) depicts these tunnel junction designs, consisting of:

1) $GaAs_{0.73}Sb_{0.27}$:C/$Ga_{0.70}In_{0.30}As$:Se (baseline)
2) $GaAs_{0.73}Sb_{0.27}$:C/$Ga_{0.22}In_{0.78}P$:Se
3) $Al_{0.30}Ga_{0.41}In_{0.29}As$:C/$Al_{0.30}Ga_{0.41}In_{0.29}As$:Se.

Fig. 5(b) shows the IQE for three tandems that employ these tunnel junctions. The all-AlGaInAs tunnel junction is highly transparent, with a peak IQE of ~95% in the bottom cell, while the baseline GaAsSb/GaInAs tunnel junction is the most absorbing, with IQE as low as ~85% at shorter wavelengths. The IQE is positively sloped from low to higher wavelengths, characteristic of parasitic absorption in the device stack. The GaAsSb/GaInP tunnel junction absorbs some light in the GaAsSb layer, yielding intermediate IQE height.

We performed flash concentrator measurements on these cells to test each tunnel junction at high current density. Fig. 5(c)-(e) shows the flash J-V curves for each tandem at multiple different light intensities. We note that the spectrum produced by the Xe flash lamp overdrives the top cell, meaning that the V_{OC} and especially the fill factor are not representative of operation under the TPV spectrum. This measurement provides a valid test for the tunnel junctions, however. The GaAsSb/GaInAs tunnel junction performs well up to 5.55 A/cm^2 then suffers a breakdown at higher current-density. The GaAsSb/GaInP tunnel junction does not exhibit tunnel junction breakdown up to the highest current-density of 12.2 A/cm^2. The all-AlGaInAs tunnel junction exhibits an internal resistive barrier[35] at all concentrations that severely limits the fill factor, despite being the most transparent tunnel junction. We were able to achieve up to $2x10^{19}$ cm^{-3} n-type doping in this material,

but (Al)GaInAs is difficult to p-dope with carbon, and so we could only reach a p-doping level of $2x10^{18}$ cm^{-3}.[36,37] Clearly this level is not high enough to promote tunneling through the diode. We attempted to dope this material with Zn, but a resistive barrier again developed near V_{OC} at even one-sun (not shown), likely due to the high diffusivity of Zn[35] reducing the doping concentration in the tunnel junction. Thus, the GaAsSb/GaInP tunnel junction presently offers the best combination of transparency and high-current-density tunneling performance. P-doping in the mid-10^{19} cm^{-3} level is achievable in GaAsSb with carbon, and were able to n-dope GaInP to that a similar level with Se. GaInP suffers from the same C-doping and Zn-diffusion challenges as (Al)GaInAs, however, precluding a ready solution for the p-type side of the tunnel junction with sufficient transparency. A transparent, p++ tunnel junction layer is the subject of further development.

D. IDEAL TPV EFFICIENCY ESTIMATE

In this last section we deduce estimates of the tandem device efficiency and the TPV system efficiency under the 2150°C radiator spectrum. We estimate the output power from high concentration J-V data, and the absorbed power by means of the reflectance data.

A tunable high intensity pulsed solar simulator (T-HIPSS) was used to collect J-V curves at variable irradiances. The T-HIPSS uses a long-arc Xe flash bulb in combination with filters and dielectric mirrors to modify the spectrum incident on the devices. The incident spectrum during J-V measurement is adjusted to simulate the 2150 °C TPV reference spectrum (hereafter the "TPV spectrum" for short) by matching the ratio

of photocurrents between junctions under the simulator spectrum to the ratio of photocurrents under the reference spectrum, as is typical for a multijunction solar PV measurement.[38] In this way, the balance of photocurrents between junctions is correct even though the simulator spectrum is not identical to the reference spectrum, and so the FF is not inflated.[39]
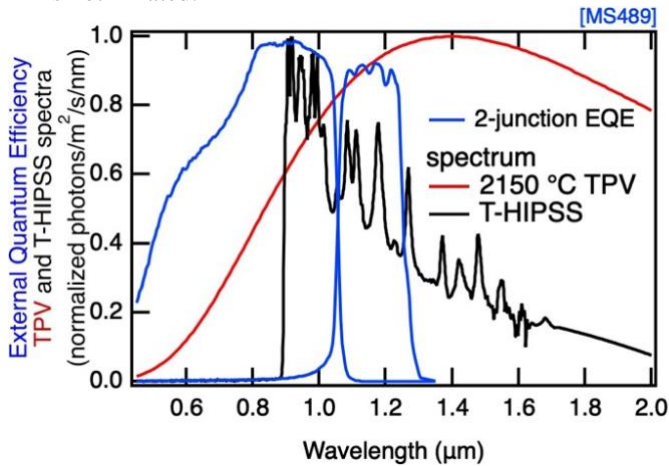

Fig. 6 Comparison of the 2150 °C TPV spectrum (red) with the T-HIPSS simulator spectrum (black), both normalized to unity. The EQE of the tandem is overlaid, highlighting the portion of the spectrum used by the device.

Compared to the TPV spectrum, the unadjusted spectrum from the Xe flash bulb contains excess short wavelength light. Gross spectral adjustment was accomplished using a double-side polished GaAs substrate with anti-reflection coatings on both sides to remove wavelengths shorter than 880 nm, and minor adjustments were made using dielectric mirrors. The photocurrent ratio, R_{ij}, which is the ratio of the effective irradiance incident on each subcell, describes the accuracy of the simulated spectrum and is measured using reference cells and spectral mismatch factors.[38] The spectrum was adjusted until $R_{ij} = 1.00$, meaning each junction received the correct photocurrent within 1% error. Figure 6 shows the measured simulator spectrum compared to the reference TPV spectrum. The external quantum efficiency of the tandem device MS489 after application of an anti-reflection coating is also overlaid.

The irradiance P_I of the TPV reference spectrum is $P_I =118.2$ W/cm².[4] Because the T-HIPSS test spectrum is not identical to the TPV spectrum, we use the device as its own reference cell, deducing the effective irradiance under the TPV spectrum—for any given J-V measurement under the test spectrum—from the J_{SC} of the J-V measurement. Integrating the measured EQE in Fig. 6 against the TPV spectrum gives $J_{SC} = 15.5$ A/cm² and 12.9 A/cm² for the top and bottom junctions respectively, so the J_{SC} for the series-limited two-junction device under the TPV spectrum is $J_{SC,TPV} = 12.9$ A/cm². The fractional effective irradiance f_E at any other intensity is therefore $f_E = J_{SC} / J_{SC,TPV}$, and the effective irradiance $P_{I,effective} = f_E P_I$.

The resulting V_{OC} and fill factor of this device based on T-HIPSS flash measurements are shown as a function of the measured J_{SC} in panels (a) and (b) of Fig. 7. The fractional effective irradiance f_E corresponding to J_{SC} is indicated along the top axis. The cell-level efficiency η_{cell} is then

$$\eta_{cell} = \frac{P_{cell}}{P_{I,effective}} = \frac{V_{OC}J_{SC}FF}{f_E P_I} \qquad (1)$$

Figure 7(c) shows the resulting values for η_{cell}, which reaches a maximum of 15.1% efficiency at a current density of 3.86 mA/cm², corresponding to an effective irradiance level $f_E = 3.86/12.9 = 29.9\%$ of the TPV spectrum irradiance. Note that the cell efficiency is measured relative to the full wavelength range of the incident spectrum.

The TPV efficiency η_{TPV} differs from the cell efficiency in that the portion P_R of the incident power P_I that is reflected back to the radiator is not considered a loss. In the idealized case of unity view factors and no parasitic (e.g. convective) losses,[6]

$$\eta_{TPV}^{ideal} = \frac{P_{cell}}{P_I - P_R} = \frac{P_I}{P_I - P_R}\eta_{cell}. \qquad (2)$$

This calculation requires broadband measurement of the device reflectance for a wide range of above- and sub-bandgap wavelengths. The wavelengths <1.24 µm were measured during EQE measurement with a calibrated photodiode, while the wavelength range >2.5µm was measured by normal incidence FTIR microscopy. We modeled the FTIR data using a simple Drude model and extrapolated the model to shorter wavelengths, to fill in the gap between the two measurements (See Appendix). While not as precise as a complete measurement, this procedure is sufficient for the estimates provided in this section.

Integrating the reflectivity of the device (MS489) against the TPV spectrum, we find $P_R =73.5$ W/cm², from which we can calculate η_{TPV}^{ideal} as shown in Fig. 7(d) as a function of J_{SC} on the bottom x-axis and f_E on the top x-axis. η_{TPV}^{ideal} increases with current density, as expected, peaking at ~39.9% at $f_E = 29.9\%$. This is a somewhat artificial operating condition since we expect that the TPV cell would be exposed to the full intensity of the emitter spectrum rather than an attenuated spectrum of the same shape. The peak efficiency is not representative of the efficiency under the full TPV irradiance due to series resistance losses. Because the T-HIPSS is only capable of accurately reproducing the TPV spectrum up to about 70% of the full irradiance, we cannot directly measure the efficiency at full irradiance, but we can extrapolate the efficiency to full irradiance as follows. The dashed lines in panels (a)-(c) show a fit to the T-HIPSS data following ref. 24, and we use the fit to extrapolate an estimated TPV efficiency of $\eta_{TPV}^{ideal}= 36\%$ under the full irradiance of the 2150°C spectrum. The power loss due to series resistance is significant at this current density, indicating that optimization of this parameter could yield large increases in TPV efficiency. A very simple but reasonable way to estimate the potential efficiency at high current density is to linearly extrapolate the efficiency vs log(J_{SC}) curve from the lower-J_{SC} region where series resistance is not significant; such extrapolation gives an estimate of η_{TPV}^{ideal}~43% for this device, even without any other optimizations, if series resistance can be mitigated sufficiently.
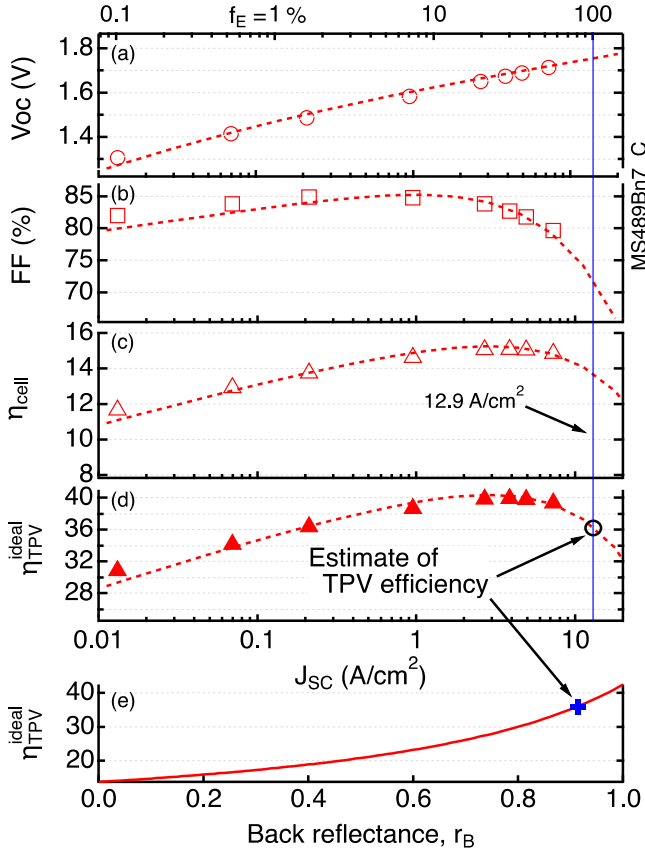
Fig. 7 Estimate of TPV efficiency. (a-b) V_{OC} and FF as measured on the T-HIPSS, with a fit following the model in ref. [24]. (c) Cell efficiency under the TPV spectrum. (d) Ideal TPV system efficiency. The vertical blue line indicates full-irradiance current density of 12.9 mA/cm². (e) Estimated ideal TPV efficiency for varying back reflectivity. The circle in (d) and the cross in (e) indicate the ~36% TPV efficiency estiate for the present cell, MS489.

Finally, we explore the potential benefits of improving the sub-bandgap reflectance by suitable engineering of the back-side reflector.[40] We note that the present device uses broad-area electroplated Au back contact that has not been optimized in any way. We write the incident and reflected irradiances P_I and P_R as the sums of their above-bandgap and below-bandgap parts: $P_I = P_{I,sub} + P_{I,above}$ and $P_R = P_{R,sub} + P_{R,above}$. We can then define the power-weighted sub-bandgap reflectance $r_b = P_{R,sub}$ / $P_{I,sub}$. With this we can rewrite the TPV efficiency η_{TPV}^{ideal} as a function of sub-bandgap reflectance r_b,

$$\eta_{TPV}^{ideal}(r_b) = \frac{P_I}{P_I - P_R}\eta_{cell} = \frac{P_I}{P_I - P_{R,above} - r_b P_{I,sub}}\eta_{cell} \quad (3)$$

Integrating the above- and below-bandgap parts of the incident and reflected TPV spectrum, we get $P_{I,sub}$ = 78.3 W/cm², $P_{R,above}$ =1.90 W/cm², $P_{R,sub}$ = 71.6 W/cm², and r_b = $P_{R,sub}$ / $P_{I,sub}$ = 0.914 = 91.4% for our cell. If we think of the sub-bandgap reflectance and thus r_b as quantities that we can vary experimentally with better back reflectors, we can then plot η_{TPV}^{ideal} (r_b) as shown in Fig. 7(e). The cross marks the value of η_{TPV}^{ideal}=36% corresponding to the measured r_b =91.4%. The figure shows that η_{TPV}^{ideal} rises rapidly with r_b: the same cell but

with r_b = 98%, an aggressive yet realistic target, would have η_{TPV}^{ideal}~40.8%. Combining this improvement in r_b with the series resistance mitigation described above would yield η_{TPV}^{ideal}~49%. Finally, optimization of the device V_{OC} and quantum efficiency described earlier is by no means complete; a small improvement of either, combined with the improvements to r_b and series resistance, would lead to η_{TPV}^{ideal}>50%.

IV. CONCLUSION

We demonstrated an inverted metamorphic two-junction 1.2/1.0 eV $Al_{0.14}Ga_{0.57}In_{0.29}As$/$Ga_{0.70}In_{0.30}As$ device in which both junctions were lattice-mismatched to the substrate but possessed the same lattice constant. This unique device architecture enabled removal of the graded buffer, increasing short wavelength carrier collection and eliminating potential free-carrier absorption in that thick, highly doped device region. This device structure is uniquely optimized for thermal energy grid storage applications. To enable this device, we developed high-quality metamorphic AlGaInAs for the high bandgap top cell, optimized by using growth conditions that minimize oxygen incorporation. An enabling metamorphic front contact layer and GaAsSb/GaInP tunnel junction robust at high current-density were also developed. A tandem device was characterized under an adjustable high-intensity pulsed simulator that simulated the 2150°C TPV blackbody spectrum. The device exhibited an estimated ideal TPV efficiency of 39.9% at a 30% fractional effective irradiance, and 36% at full TPV irradiance. We discussed a roadmap to significant further improvement in efficiency with improvements to the sub-bandgap weighted reflectance, reductions to the series resistance of the device, and further device performance improvements.

APPENDIX – SUB-BANDGAP REFLECTANCE MODELING

Due to limitations in our ability to measure the device reflectivity with a single tool, we lacked reflectance data for the tandem device MS489 in the sub-bandgap region between 1.24 and 2.50 µm. We modeled the data above 2.50 µm, measured experimentally by FTIR, and then extrapolated to 1.24 µm to bridge the gap. The transfer matrix method[41] was used to model the reflectance, and the Drude model was used to calculate the dielectric function in the region below the bandgap, which was assumed to be dominated by free-carriers. The Drude model describes the contribution of free carriers to the frequency-dependent dielectric function, ε, in metals or heavily doped semiconductors[42] and is calculated by:

$$\varepsilon = \varepsilon_{core} - \frac{Ne^2}{m\varepsilon_0(\omega^2 + i\gamma\omega)}. \qquad (A.I)$$

N is the doping concentration of electrons or holes, ε_{core} is the portion of the dielectric function not influenced by free carriers, ε_0 is the vacuum permittivity, m is the effective mass of electrons or holes, e is the electron charge, and ω is the angular frequency. The damping frequency, γ, is related to the carrier mobility, μ, by the DC electrical conductivity as

$$\sigma_{dc} = \frac{Ne^2}{m\gamma} = Ne\mu. \qquad (A.II)$$

The optical properties, refractive index n and extinction coefficient k, can be calculated from the real, ε', and imaginary, ε'', portions of the dielectric function

$$\varepsilon = (n + ik)^2 = \varepsilon' + i\varepsilon''. \qquad (A.III)$$

The transfer matrix model was fit to the FTIR data by considering a single Drude layer representative of all the cell layers and an optically thick gold back reflector. Gold optical properties were taken from.[43] The fitting parameters were N, μ, ε_{core}, m, and the Drude layer thickness. The single Drude layer was found to capture the free carrier absorption well, and the model was used for the purpose of extrapolating the FTIR reflectance to 1.24 µm. Fig. 8 shows the merged reflectance used in the TPV system efficiency estimate in section III.D, which contains the above bandgap region measured by a calibrated photodiode and the sub-bandgap portions estimated by the model and measured by FTIR.
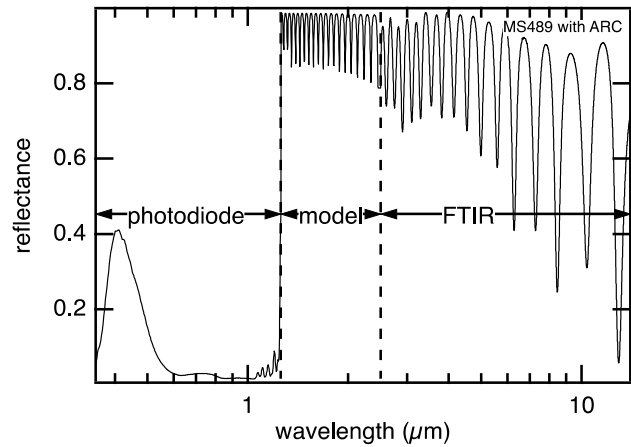

Fig. 8 Merged device reflectance for MS489 consisting of measured (photodiode, FTIR) and modeled components. This reflectance is used to calculate TPV efficiency in section III.D.

DATA AVAILABILITY

The data that support the findings of this study are available within the article.

REFERENCES

1. R. M. France, J. F. Geisz, I. García, M. A. Steiner, W. E. McMahon, D. J. Friedman, T. E. Moriarty, C. Osterwald, J. S. Ward, and A. Duda, IEEE Journal of Photovoltaics **6,** 578 (2016).
2. J. F. Geisz, R. M. France, K. L. Schulte, M. A. Steiner, A. G. Norman, H. L. Guthrey, M. R. Young, T. Song, and T. Moriarty, Nature Energy (2020).
3. J. F. Geisz, M. A. Steiner, N. Jain, K. L. Schulte, R. M. France, W. E. McMahon, E. E. Perl, and D. J. Friedman, IEEE Journal of Photovoltaics **8,** 626 (2018).
4. C. Amy, H. R. Seyf, M. A. Steiner, D. J. Friedman, and A. Henry, Energy & Environmental Science **12,** 334 (2019).
5. A. Henry, R. Prasher, and A. Majumdar, Nature Energy, 1 (2020).
6. T. Coutts, Renewable and sustainable energy reviews **3,** 77 (1999).
7. W. Walukiewicz, J. Lagowski, L. Jastrzebski, P. Rava, M. Lichtensteiger, C. Gatos, and H. Gatos, Journal of Applied Physics **51,** 2659 (1980).
8. W. Dumke, M. Lorenz, and G. Pettit, Physical Review B **1,** 4668 (1970).
9. H. Iber, E. Peiner, and A. Schlachetzki, Journal of applied physics **79,** 9273 (1996).
10. D. Vignaud and J. Farvacque, Journal of applied physics **65,** 1261 (1989).
11. R. M. France, P. Espinet-Gonzalez, B. B. Haidet, K. Mukherjee, H. L. Guthrey, H. A. Atwater, and D. Walker, IEEE Journal of Photovoltaics **10,** 103 (2019).
12. K. L. Schulte, H. L. Guthrey, R. M. France, and J. F. Geisz, IEEE Journal of Photovoltaics **10,** 109 (2019).
13. S. Heckelmann, D. Lackner, C. Karcher, F. Dimroth, and A. W. Bett, IEEE Journal of Photovoltaics **5,** 446 (2014).
14. S. Heckelmann, D. Lackner, F. Dimroth, and A. Bett, Journal of Crystal Growth **464,** 49 (2017).
15. M. Goorsky, T. Kuech, F. Cardone, P. Mooney, G. Scilla, and R. Potemski, Applied physics letters **58,** 1979 (1991).
16. M. S. Leite, R. L. Woo, W. D. Hong, D. C. Law, and H. A. Atwater, Applied Physics Letters **98,** 093502 (2011).
17. B. L. Smith, Z. S. Bittner, S. D. Hellstroem, G. T. Nelson, M. A. Slocum, A. G. Norman, D. V. Forbes, and S. M. Hubbard, Progress in Photovoltaics: Research and Applications **25,** 706 (2017).
18. W. Guter, F. Dunzer, L. Ebel, K. Hillerich, W. Köstler, T. Kubera, M. Meusel, B. Postels, and C. Wächter, in *Space solar cells–3g30 and next generation radiation hard products*, 2017 (EDP Sciences), p. 03005.
19. X. Liu, C. Fetzer, E. Rehder, H. Cotal, S. Mesropian, D. Law, and R. King, Journal of crystal growth **352,** 186 (2012).

[20] I. Mathews, D. O'Mahony, A. Gocalinska, M. Manganaro, E. Pelucchi, M. Schmidt, A. P. Morrison, and B. Corbett, Applied Physics Letters **102,** 033906 (2013).

[21] J. F. Geisz, A. X. Levander, A. G. Norman, K. M. Jones, and M. J. Romero, Journal of Crystal Growth **310,** 2339 (2008).

[22] A. Duda, J. S. Ward, and M. Young, "Inverted Metamorphic Multijunction (IMM) Cell Processing Instructions," (2012).

[23] J. F. Geisz, M. A. Steiner, I. Garcia, S. R. Kurtz, and D. J. Friedman, Applied Physics Letters **103,** 041118 (2013).

[24] J. F. Geisz, M. A. Steiner, I. García, R. M. France, W. E. McMahon, C. R. Osterwald, and D. J. Friedman, IEEE Journal of Photovoltaics **5,** 1827 (2015).

[25] U. Rau, Physical Review B **76,** 085303 (2007).

[26] E. E. Perl, J. Simon, J. F. Geisz, M. L. Lee, D. J. Friedman, and M. A. Steiner, IEEE Journal of Photovoltaics **6,** 1345 (2016).

[27] T. Kuech, R. Potemski, F. Cardone, and G. Scilla, Journal of electronic materials **21,** 341 (1992).

[28] J. A. Dean, *Lange's handbook of chemistry* (New york; London: McGraw-Hill, Inc., 1999).

[29] J.-W. Huang and T. F. Kuech, Applied physics letters **65,** 604 (1994).

[30] Y. Sun, A. Perna, and P. Bermel, IEEE Journal of Photovoltaics **9,** 437 (2019).

[31] W. Shockley and H. J. Queisser, Journal of Applied Physics **32,** 510 (1961).

[32] K. Yu, W. Walukiewicz, W. Shan, J. Ager III, J. Wu, E. Haller, J. Geisz, D. Friedman, and J. Olson, Physical Review B **61,** R13337 (2000).

[33] M. A. Steiner, J. F. Geisz, R. C. Reedy, and S. Kurtz, in *A direct comparison of inverted and non-inverted growths of GaInP solar cells*, 2008 (IEEE), p. 1.

[34] I. García, J. Geisz, R. France, J. Kang, S.-H. Wei, M. Ochoa, and D. Friedman, Journal of Applied Physics **116,** 074508 (2014).

[35] K. L. Schulte, M. A. Steiner, M. R. Young, and J. F. Geisz, IEEE Journal of Photovoltaics **9,** 167 (2018).

[36] S. Stockman, A. Hanson, S. Lichtenthal, M. Fresina, G. Höfler, K. Hsieh, and G. Stillman, Journal of electronic materials **21,** 1111 (1992).

[37] C. Caneau, R. Bhat, S. Goswami, and M. Koza, Journal of electronic materials **25,** 491 (1996).

[38] K. Emery, Handbook of Photovoltaic Science and Engineering**,** 797 (2011).

[39] C. R. Osterwald, M. W. Wanlass, T. Moriarty, M. A. Steiner, and K. A. Emery, in *Concentrator cell efficiency measurement errors caused by unfiltered xenon flash solar simulators*, 2014 (American Institute of Physics), p. 149.

[40] T. Burger, D. Fan, K. Lee, S. R. Forrest, and A. Lenert, ACS Photonics **5,** 2748 (2018).

[41] G. Chen, *Nanoscale energy transport and conversion: a parallel treatment of electrons, molecules, phonons, and photons* (Oxford University Press, 2005).

[42] M. Dresselhaus, G. Dresselhaus, S. B. Cronin, and A. G. Souza Filho, in *Solid State Properties* (Springer, 2018), p. 329.

[43] R. L. Olmon, B. Slovick, T. W. Johnson, D. Shelton, S.-H. Oh, G. D. Boreman, and M. B. Raschke, Physical Review B **86,** 235147 (2012).